UC Irvine
UC Irvine Previously Published Works

Title

Quantitative optical tomography of sub-surface heterogeneities using spatially modulated structured light

Permalink

Journal

ISSN

Authors

Konecky, Soren D
Mazhar, Amaan
Cuccia, David
et al.

Publication Date

DOI

Copyright Information

Peer reviewed

Quantitative optical tomography of sub-surface heterogeneities using spatially modulated structured light

**Soren D. Konecky,[1] Amaan Mazhar,[1] David Cuccia,[2]
Anthony J. Durkin,[1] John C. Schotland,[3] Bruce J. Tromberg[1,*]**

[1]*Laser Microbeam and Medical Program (LAMMP),
Beckman Laser Institute, University of California - Irvine, 1002 Health Sciences Road, Irvine, CA 92617, USA*
[2]*Modulated Imaging Inc., 1002 Health Sciences Road, Irvine, CA 92617, USA*
[3]*Department of Bioengineering, University of Pennsylvania, Philadelphia,PA 19104, USA*
[*]bjtrombe@uci.edu

Abstract: We present a wide-field method for obtaining three-dimensional images of turbid media. By projecting patterns of light of varying spatial frequencies on a sample, we reconstruct quantitative, depth resolved images of absorption contrast. Images are reconstructed using a fast analytic inversion formula and a novel correction to the diffusion approximation for increased accuracy near boundaries. The method provides more accurate quantification of optical absorption and higher resolution than standard diffuse reflectance measurements.

©2009 Optical Society of America

OCIS codes: (110.0113) Imaging through turbid media; (170.3880) Medical and biological imaging; (170.6510) Spectroscopy, tissue diagnostics

References and links

1. A. P. Gibson, J. C. Hebden, and S. R. Arridge, "Recent advances in diffuse optical imaging," Phys. Med. Biol. **50**(4), R1–R43 (2005).
2. B. J. Tromberg, B. W. Pogue, K. D. Paulsen, A. G. Yodh, D. A. Boas, and A. E. Cerussi, "Assessing the future of diffuse optical imaging technologies for breast cancer management," Med. Phys. **35**(6), 2443–2451 (2008).
3. J. C. Hebden, "Advances in optical imaging of the newborn infant brain," Psychophysiology **40**(4), 501–510 (2003).
4. V. Ntziachristos, J. Ripoll, L. V. Wang, and R. Weissleder, "Looking and listening to light: the evolution of whole-body photonic imaging," Nat. Biotechnol. **23**(3), 313–320 (2005).
5. D. J. Cuccia, F. Bevilacqua, A. J. Durkin, and B. J. Tromberg, "Modulated imaging: quantitative analysis and tomography of turbid media in the spatial-frequency domain," Opt. Lett. **30**(11), 1354–1356 (2005).
6. A. Bassi, C. D'Andrea, G. Valentini, R. Cubeddu, and S. Arridge, "Temporal propagation of spatial information in turbid media," Opt. Lett. **33**(23), 2836–2838 (2008).
7. A. Joshi, W. Bangerth, K. Hwang, J. C. Rasmussen, and E. M. Sevick-Muraca, "Fully adaptive FEM based fluorescence optical tomography from time-dependent measurements with area illumination and detection," Med. Phys. **33**(5), 1299–1310 (2006).
8. D. J. Cuccia, F. Bevilacqua, A. J. Durkin, F. R. Ayers, and B. J. Tromberg, "Quantitation and mapping of tissue optical properties using modulated imaging," J. Biomed. Opt. **14**(2), 024012 (2009).
9. D. Abookasis, C. C. Lay, M. S. Mathews, M. E. Linskey, R. D. Frostig, and B. J. Tromberg, "Imaging cortical absorption, scattering, and hemodynamic response during ischemic stroke using spatially modulated near-infrared illumination," J. Biomed. Opt. **14**(2), 024033 (2009).
10. D. J. Cuccia, D. Abookasis, R. D. Frostig, and B. J. Tromberg, "Quantitative in vivo imaging of tissue absorption, scattering, and hemoglobin concentration in rat cortex using spatially-modulated structured light," in *In Vivo Optical Imaging of Brain Function,* 2nd ed., R. D. Frostig, ed. (CRC, 2009).
11. J. R. Weber, D. J. Cuccia, A. J. Durkin, and B. J. Tromberg, "Noncontact imaging of absorption and scattering in layered tissue using spatially modulated structured light," J. Appl. Phys. in press.
12. V. A. Markel, and J. C. Schotland, "Symmetries, inversion formulas, and image reconstruction for optical tomography," Phys. Rev. E Stat. Nonlin. Soft Matter Phys. **70**(5), 056616 (2004).
13. J. C. Schotland, and V. A. Markel, "Inverse scattering with diffusing waves," J. Opt. Soc. Am. A **18**(11), 2767–2777 (2001).
14. S. D. Konecky, G. Y. Panasyuk, K. Lee, V. Markel, A. G. Yodh, and J. C. Schotland, "Imaging complex structures with diffuse light," Opt. Express **16**(7), 5048–5060 (2008).

15. Z. M. Wang, G. Y. Panasyuk, V. A. Markel, and J. C. Schotland, "Experimental demonstration of an analytic method for image reconstruction in optical diffusion tomography with large data sets," Opt. Lett. **30**(24), 3338–3340 (2005).
16. V. Lukic, V. A. Markel, and J. C. Schotland, "Optical tomography with structured illumination," Opt. Lett. **34**(7), 983–985 (2009).
17. G. Y. Panasyuk, V. A. Markel, and J. C. Schotland, "Superresolution and corrections to the diffusion approximation in optical tomography," Appl. Phys. Lett. **87**(10), 101111 (2005).
18. V. A. Markel, and J. C. Schotland, "Inverse problem in optical diffusion tomography. II. Role of boundary conditions," J. Opt. Soc. Am. A **19**(3), 558–566 (2002).
19. V. A. Markel, V. Mital, and J. C. Schotland, "Inverse problem in optical diffusion tomography. III. Inversion formulas and singular-value decomposition," J. Opt. Soc. Am. A **20**(5), 890–902 (2003).
20. A. C. Kak, and M. Slaney, *Principles of Computerized Imaging* (IEEE, 1988).
21. *http://www.bli.uci.edu/ntroi/phantoms.php*, retrieved April 24th, 2009.
22. F. Bevilacqua, A. J. Berger, A. E. Cerussi, D. Jakubowski, and B. J. Tromberg, "Broadband absorption spectroscopy in turbid media by combined frequency-domain and steady-state methods," Appl. Opt. **39**(34), 6498–6507 (2000).
23. H. P. Tuan, O. Coquoz, J. B. Fishkin, E. Anderson, and B. J. Tromberg, "Broad bandwidth frequency domain instrument for quantitative tissue optical spectroscopy," Rev. Sci. Instrum. **71**(6), 2500–2513 (2000).
24. B. W. Pogue, T. O. McBride, J. Prewitt, U. L. Osterberg, and K. D. Paulsen, "Spatially variant regularization improves diffuse optical tomography," Appl. Opt. **38**(13), 2950–2961 (1999).
25. J. C. Schotland, and V. A. Markel, "Fourier-Laplace structure of the inverse scattering problem for the radiative transport equation," Inverse Problems and Imaging **1**, 147–154 (2007).
26. G. Y. Panasyuk, J. C. Schotland, and V. A. Markel, "Radiative Transport Equation in Rotated Reference Frames," J. Phys. A **39**(1), 115–137 (2006).
27. V. A. Markel, "Modified spherical hamonics method for solving the radiative transport equation," Waves Random Media **14**(1), L13–L19 (2004).

1. Introduction

Optical tomography with multiply scattered light [1] is a rapidly growing field with applications ranging from human breast [2] and brain [3], to small animals [4]. Recently, in an effort to image large fields of view quickly, we and others have begun projecting spatially extended patterns of light on tissue, eliminating the need to use large arrays of optical fibers or raster scan a collimated beam [5–7]. In particular, it has been experimentally demonstrated that by projecting sinusoidal patterns of light onto tissue, one can determine the tissue's optical properties by measuring the relative decay of spatial patterns of differing frequencies [5,8]. This technique has been applied to imaging stroke in the rat cerebral cortex [9], visualizing cortical spreading depression [10], and assessing layered structures in skin [11]. The principle advantages of projecting a spatially extended source are that one can image a large field of view quickly, it is non-contact, inexpensive, and it eliminates the need for detectors with a wide dynamic range since all detectors are close to a spatially extended source. This is especially important for reflectance measurements, since the remitted light intensity due to a point source decays by many orders of magnitude within millimeters.

In our previous work using a spatially modulated light source, tissue optical properties were determined by fitting to a model of light propagation that assumed the tissue was a homogeneous or a layered structure. The data acquired by each detector (i.e. each pixel on the CCD array) was analyzed independently of all the other detectors. This approach tacitly assumed that tissue optical properties (within layers) did not vary with depth, and that neighboring volumes of tissue did not affect the light intensity measured at a given pixel. This approach is sufficient for samples in which optical property changes are both gradual and located near the surface. However, we expect images of small buried objects to appear blurred, and to underestimate optical property changes. This is because each detector samples a volume much larger than the absorber, and because each detector is primarily sensitive to the optical properties at the surface. Thus, the optical properties assigned to any region of tissue are in fact the average values for a much larger region, and this average is highly weighted by the optical properties at the surface. The goal of image reconstruction is ameliorate this partial volume effect, by modeling the sensitivity of each measurement to the entire tissue volume.

The theoretical framework for describing the propagation of plane waves of diffuse light and reconstructing images of sub-surface heterogeneities in the spatial Fourier domain have

been known for several years [12,13]. However, the original reconstructed images using these methods were acquired by raster scanning a collimated laser beam and numerically taking a Fourier transform of the resulting data [14,15]. Recently, an algorithm was proposed for reconstructing three-dimensional images directly from measurements made by illuminating tissue with sinusoidal patterns [16]. The algorithm takes advantage of the insight that illuminating with sinusoidal functions of different frequencies is theoretically equivalent to raster scanning a point source and then taking a Fourier transform of the data with respect to the source positions.

In this manuscript we experimentally validate the tomographic approach of Ref [16]. using tissue simulating phantoms with buried heterogeneities resembling superficial veins. We also modify this approach by implementing a novel correction to the diffusion approximation which gives increased accuracy in the reconstructed images near the tissue surface [17]. We quantitatively measure the optical absorption of buried objects, determine their relative depths, and image them with higher resolution than is obtained by fitting to a homogeneous model.

2. Methods

2.1 Theory

The propagation of multiply scattered photons in biological tissue is governed by the radiative transport equation (RTE). For a continuous-wave light source at a single wavelength the RTE for light appears as:

$$\hat{\mathbf{s}} \cdot \nabla I(\mathbf{r},\hat{\mathbf{s}}) + (\mu_a + \mu_s)I(\mathbf{r},\hat{\mathbf{s}}) - \mu_s \int d^2 s' A(\hat{\mathbf{s}},\hat{\mathbf{s}}')I(\mathbf{r},\hat{\mathbf{s}}') = S(\mathbf{r},\hat{\mathbf{s}}) . \qquad (1)$$

Here $I(\mathbf{r},\hat{\mathbf{s}})$ is the specific intensity, μ_a is the absorption coefficient, μ_s is the scattering coefficient, $A(\hat{\mathbf{s}},\hat{\mathbf{s}}')$ is the scattering kernel, and $S(\mathbf{r},\hat{\mathbf{s}})$ is the source. The diffusion approximation to the RTE is obtained by expanding $I(\mathbf{r},\hat{\mathbf{s}})$ to first order in $\hat{\mathbf{s}}$ resulting in an approximation for $I(\mathbf{r},\hat{\mathbf{s}})$ that consists of both a photon density and a current term:

$$I(\mathbf{r},\hat{\mathbf{s}}) = \frac{c}{4\pi}\Phi(\mathbf{r}) + \frac{3}{4\pi}\mathbf{J}\cdot\hat{\mathbf{s}} . \qquad (2)$$

Near boundaries, where the specific intensity is not isotropic, both the density and current terms are important. Retaining both terms, the Green's function to the RTE can be approximated in terms of the Greens function for the diffusion equation as [12]:

$$G(\mathbf{r},\hat{\mathbf{s}},\mathbf{r}',\hat{\mathbf{s}}') = \frac{c}{4\pi}(1+\ell^*\hat{\mathbf{s}}\cdot\nabla_{\mathbf{r}})(1-\ell^*\hat{\mathbf{s}}'\cdot\nabla_{\mathbf{r}'})G(\mathbf{r},\mathbf{r}') , \qquad (3)$$

where c is the speed of light in the medium, $\ell^* = 1/(\mu_a + \mu_s')$, and $G(\mathbf{r},\mathbf{r}')$ is the Greens function for the diffusion equation which obeys the equation

$$[-\nabla \cdot D\nabla + c\mu_a]\, G(\mathbf{r},\mathbf{r}') = \delta(\mathbf{r}-\mathbf{r}') , \qquad (4)$$

subject to the boundary condition

$$G(\mathbf{r},\mathbf{r}') + \ell\hat{\mathbf{n}}\cdot\nabla G(\mathbf{r},\mathbf{r}') = 0 . \qquad (5)$$

Here $D = c\ell^*/3$ is the diffusion coefficient, ℓ is the extrapolation length, and $\hat{\mathbf{n}}$ is the outward pointing unit normal. As demonstrated in Ref [18], the Greens function for the diffusion equation in a semi-infinite medium can be decomposed into plane waves according to

$$G(\mathbf{r}, \mathbf{r}') = \frac{1}{(2\pi)^2} \int d^2q \; g(\mathbf{q}, z, z') \exp[i(\mathbf{q} \cdot (\boldsymbol{\rho}' - \boldsymbol{\rho}))] \;, \tag{6}$$

where the Fourier component

$$g(\mathbf{q}, z, z') = \frac{\ell}{D} \frac{\exp[-Q(\mathbf{q}) \,|\, z - z'|]}{Q(\mathbf{q})\ell + 1} \tag{7}$$

governs the decay of spatial waves as they propagate to or from the surface of the tissue. The decay rate $Q(\mathbf{q}) = (c\mu_a / D + \mathbf{q}^2)^{1/2}$ is determined by the optical properties of the medium and the frequency of the spatial wave.

Our goal is to determine the spatial variations in absorption by projecting sinusoidal patterns of differing frequencies and phases on the sample, and measuring the spatially varying intensity of the remitted light at the surface. The change in specific intensity due to a perturbation of the absorption coefficient in the medium obeys to first order the following integral equation:

$$\varphi(\mathbf{k}, \mathbf{r}_d, \hat{\mathbf{s}}_d) = \int d^3r \; d^2s \; I(\mathbf{r}, \hat{\mathbf{s}}) \; G(\mathbf{r}, \hat{\mathbf{s}}, \mathbf{r}_d, \hat{\mathbf{s}}_d) \; \delta\mu_a(\mathbf{r}) \;, \tag{8}$$

where $\varphi(\mathbf{k}, \mathbf{r}_d, \hat{\mathbf{s}}_d)$ is the experimentally measured data function at detector location $\mathbf{r}_d$, in direction $\hat{\mathbf{s}}_d$, due to a light source with spatial wave number $\mathbf{k}$. $\delta\mu_a(\mathbf{r})$ is the change in absorption, and $I(\mathbf{r}, \hat{\mathbf{s}})$ is the specific intensity do to the spatially extended source and obeys the equation

$$I(\mathbf{r}, \hat{\mathbf{s}}) = \int d^3r' d^2s' \; G(\mathbf{r}', \hat{\mathbf{s}}', \mathbf{r}, \hat{\mathbf{s}}) S(\mathbf{r}', \hat{\mathbf{s}}') \;. \tag{9}$$

In our experiment, the source consists of light which is sinusoidal in space with wave number $\mathbf{k}$, has intensity I_0, and is directed into the sample at the surface. It is described as:

$$S(\mathbf{r}, \hat{\mathbf{s}}) = I_0 \exp(i\mathbf{k} \cdot \boldsymbol{\rho}) \delta(z) \delta(\hat{\mathbf{s}} + \hat{\mathbf{n}}) \;. \tag{10}$$

By substituting Eqs. (3) and (9) into Eq. (8) and using Eqs. (5-7) and (10), Eq. (8) can be put in the form

$$\varphi(\mathbf{k}, \boldsymbol{\rho}_d) = \frac{c \, I_0}{4\pi} (1 + \frac{\ell^*}{\ell})^2 \int d^3r \; K(\mathbf{k}, \boldsymbol{\rho}_d; \mathbf{r}) \; c \; \delta\mu_a(\mathbf{r}) \;, \tag{11}$$

where

$$K(\mathbf{k}, \boldsymbol{\rho}_d; \mathbf{r}) = \frac{1}{(2\pi)^2} \int d^2q \; \kappa(\mathbf{k}, \mathbf{q}; z) \; \exp[i(\mathbf{k} - \mathbf{q}) \cdot \boldsymbol{\rho} + i\mathbf{q} \cdot \boldsymbol{\rho}_d] \;, \tag{12}$$

and

$$\kappa(\mathbf{k}, \mathbf{q}; z) = (\frac{\ell}{D})^2 [1 - \frac{\ell^{*2}}{3} (\mathbf{k} \cdot \mathbf{q} + Q(\mathbf{k}) Q(\mathbf{q}))] \frac{\exp[-(Q(\mathbf{k}) + Q(\mathbf{q})) z]}{(Q(\mathbf{k})\ell + 1)(Q(\mathbf{q})\ell + 1)} \;. \tag{13}$$

By taking a 2D Fourier transform with respect to the detector locations $\boldsymbol{\rho_d}$, Eq. (11) can be put in block diagonal form and inverted by analytical methods which have been previously described [12,19].

Note, the source function specified by Eq. (10) contains a complex exponential, while the source intensity in the actual experiment is real and positive. It has the form

$$S(\mathbf{k}, \boldsymbol{\rho}, \theta) = \frac{I_0}{2}(1 + M\cos(\mathbf{k}\cdot\boldsymbol{\rho} + \theta))\ \delta(z)\ \delta(\hat{\mathbf{s}} + \hat{\mathbf{n}})\ . \tag{14}$$

Here M and θ are the modulation depth and phase of the source. Since the diffusion equation is linear, we can obtain the data that would be generated by a source of the form of Eq. (10) by using the source described by Eq. (14). To do so, we acquire data for at least three phases, and add a linear combination of the resulting measurements of light intensity $I(\boldsymbol{\rho})$ such that the total source distribution from the three measurements equals Eq. (10). For example, using three phases ($\theta = -2\pi/3, 0, 2\pi/3$), we combine the resulting measurements as

$$I_{tot} = \frac{1}{3}(2I_2 - I_1 - I_3) + \frac{i}{\sqrt{3}}(I_1 - I_3)\ . \tag{15}$$

Due to the relatively large subsurface absorption perturbation we use the Rytov approximation [20]. In order to calculate the Rytov data function we use the standard rules for complex numbers to write I_{tot} in terms of an amplitude and phase (i.e. $I_{tot} = Ae^{i\phi}$), where for three phases

$$A = \frac{\sqrt{2}}{3}\{(I_1 - I_2)^2 + (I_2 - I_3)^2 + (I_3 - I_1)^2\}^{1/2}\ , \tag{16}$$

and

$$\phi = \tan^{-1}\{\sqrt{3}(I_1 - I_3)\big/(2I_2 - I_1 - I_3)\}\ . \tag{17}$$

Then the Rytov data function is calculated as:

$$\varphi_{Rytov} = -I_{tot}^{(0)}\{\log(A/A^{(0)}) + i(\phi - \phi^{(0)})\}\ . \tag{18}$$

This formulation differs from the usual temporal frequency domain in that the amplitude and phase represent the Fourier components in space, and not in time. The data acquired this way is equivalent to the data acquired by using point sources and then taking a Fourier transform with respect to their spatial positions.

2.2 Instrumentation

A schematic of the instrument is shown in Fig. 1. Broadband light was generated with a Newport Corporation power source (Newport Corporation, Irvine CA) and a 250 watt tungsten lamp. This light was used to illuminate a DLP Developers Kit 1024 x 768 pixel digital micro-mirror device (Texas Instrument, Dallas TX) which spatially modulated the light to be projected onto the phantom. Frequency patterns for the spatial modulation were generated using customized C# code (Modulated Imaging Inc., Irvine CA) and ALP (Application Program Interface) software. The patterned light was projected directly onto the phantoms approximately 500 mm from the projector system. Eleven frequencies evenly spaced from 0 to 1 cm^{-1} with four phases each were used. The diffuse reflected light images were acquired at 650 nm with a Nuance Multispectral Imaging System (CRi Inc., Woburn, MA) which consists of a liquid crystal tunable filter capable of acquiring at discrete wavelengths (10nm bandwidth) between 650 nm and 1100 nm, and a 1040 x 1392 pixel, front illuminated charge coupled device (CCD). A 6x6 cm field of view was acquired by the CCD using 4x4 hardware binning and an exposure time of ~100 ms. Cross-polarizers were placed at the source and detector in order to eliminate any specular reflection.
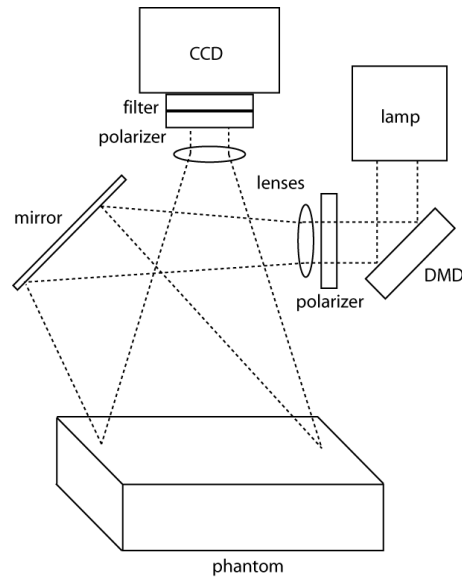
Fig. 1. Schematic of the experimental setup. Broadband light from a lamp is projected on the sample using a digital micro-mirror device (DMD) and detected at discrete wavelengths using a liquid crystal tunable filter and CCD. Crossed polarizers eliminate specular reflections.

2.3 Phantoms

Tissue simulating phantoms were made from silicone (P4, Eager Plastics, Chicago, IL), with titanium dioxide (TI-602, Atlantic Equipment Engineers, Bergenfield, NJ) used as a scattering agent, and nigrosin (Sigma, St. Louis, MO) as an absorber [21]. Optical property measurements obtained by fitting the diffuse reflectance at the different measured spatial frequencies to an analytic model for a homogeneous semi-infinite medium [5] were $\mu_a = 0.004$ mm^{-1} and $\mu_s' = 0.9$ mm^{-1} for 650 nm light. These values were calculated using standard reflectance phantoms measured previously using "gold standard" Diffuse Optical Spectroscopy (DOS), a multi-frequency, multi-distance method combining frequency-domain photon migration and broadband spectroscopy [22,23]. Phantoms were constructed with cylindrical tube shaped void(s) 1.8 mm in diameter running parallel to the surface centered at depths of 2 and 3 mm. A mixture of a fatty emulsion (Lyposin II, Abbott Laboratories, Chicago, IL), nigrosin, and water was injected into the tubes. The scattering properties of the mixture were matched to that of the silicone phantom, whereas the absorption varied so that the contrast between the tube and background material was varied from 3:1 to 100:1.

3. Results and discussion

An example of a three-dimensional reconstructed image is shown in Fig. 2. The phantom, depicted in Fig. 2(a), consisted of a single absorbing tube with an absorption contrast of 50:1. This is the absorption contrast in the near-infrared that we expect between superficial veins and the surrounding tissue. The center of the tube was located at a depth of 3 mm. Figure 2(b) is a volume rendering of the three-dimensional reconstructed absorption image. The tube surface in the volume rendering represents an isosurface of 60% of the maximum reconstructed value in the image. Individual slices through the three-dimension image at depths of 1-5 mm are shown in Fig. 2(c). At the surface the tube is not visible. The maximum amount of absorption occurs in the 1 mm slice. Absorption then decreases with depth until at a depth of 5 mm no absorption contrast is present.
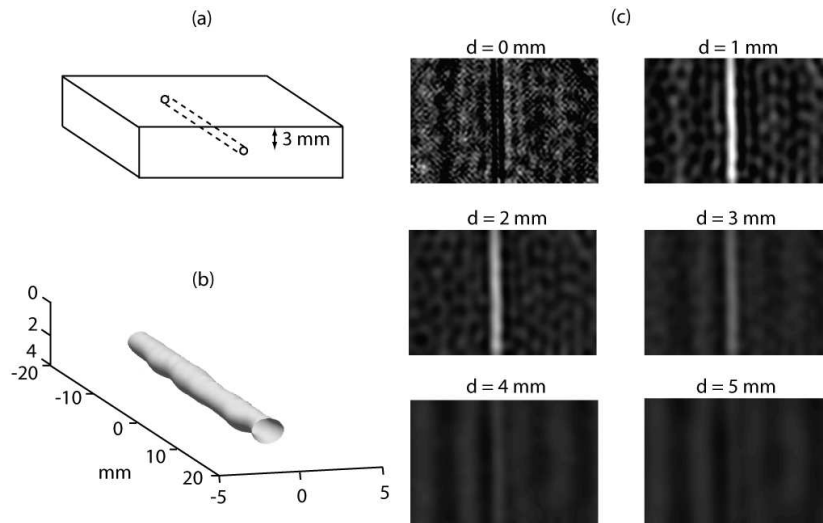
Fig. 2. Example of a reconstructed image of a single absorbing tube located 3 mm below the surface of a tissue simulating phantom. (a) Schematic of the tissue simulating phantom. (b) Volume rendering of the three-dimensional reconstructed image. (c) Slices through the reconstructed image at depths of d = 1-5 mm.

Image reconstruction leads to a significant increase in resolution compared to images created by fitting for optical properties on pixel by pixel basis while assuming a homogeneous model. Profiles of tomographic images are shown in Fig. 3. The profiles are from experiments with a single absorbing tube at depths of 2 mm (Fig. 3(a)) and 3 mm (Fig. 3(b)). In both cases the contrast in 50:1. The curves are normalized to a maximum value of one to facilitate a comparison of the two methods. The solid lines correspond to the lateral profiles of the reconstructed images. The full-width-half-maximum (FWHM) for the plots shown are 1.8 mm and 2.2 mm at depths of 2 mm and 3 mm respectively. We also measured the FWHM for tubes with contrasts ranging from 3:1 to 100:1. The FWHM ranged from 1.8 to 2.3 mm at a depth of 2 mm and from 2.2 to 3.2 mm at a depth of 3 mm, with the low contrast images having slightly lower resolution. For comparison, profiles of the images obtained by fitting pixel by pixel to a homogeneous model are shown with dotted lines. The FWHM is approximately three times larger. For the different concentrations, the FWHM determined from homogeneous model fits ranged from 4.4 to 6.8 mm at 2 mm depth, and from 5.5 to 9.5 mm at 3 mm depth.
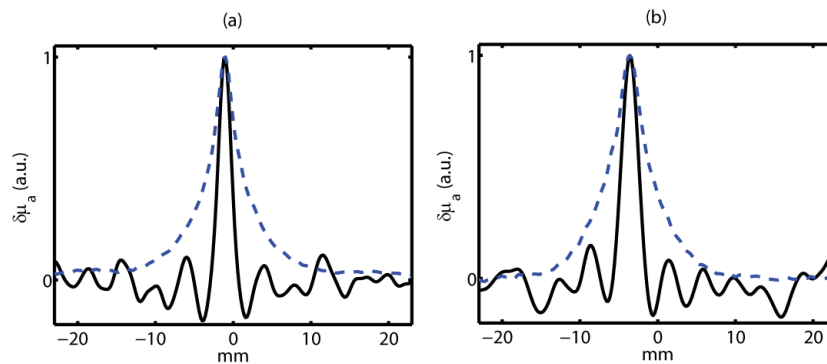

Fig. 3. Line profiles of the reconstructed images of a single absorbing tube at depths of (a) 2mm and (b) 3 mm. Solid line corresponds to tomographic reconstruction, and dotted lines correspond to pixel by pixel fitting to a homogeneous model. Curves are normalized to facilitate comparison.

The improved resolution not only allows one to distinguish between nearby absorbers, but also decreases errors in quantification due to the blurring of nearby objects in the image. As a demonstration, we imaged four absorbing tubes at a depth of 2 mm. Each tube contained the same concentration of nigrosin, with the expected contrast being 50:1. The lateral spacing between the tubes was 3, 4, and 5 mm (see Fig. 4(a)). In the reconstructed image and line profile (Fig. 4(b)) the tubes are clearly resolved and all have approximately the same reconstructed value of absorption. In contrast, for the image obtained by fitting pixel by pixel (Fig. 4(c)), the center two tubes appear to contain much more contrast than the outer tubes. This is because the image the absorption from nearby tubes, which appears broadened, is added to absorption of any given tube such that the central tubes falsely appear to have more absorption. Note, the maximum intensity also differs greatly, as images created using the homogeneous model underestimate the actual contrast by about a factor ten.

In order to quantify the ability of both imaging methods to accurately recover the amount of absorption in a small sub-surface heterogeneity, we performed titration experiments in which the expected contrast in a single tube was varied from 3:1 to 100:1. Figure 5 shows the measured contrast versus the expected contrast using both the tomographic (Fig. 5(a,c)) and pixel by pixel (Fig. 5(b,d)) methods. The depth of the absorbing tube was 2 mm for Fig. 5(a,b), and 3 mm for Fig. 5(c,d). The contrast was determined by selecting a region of interest (ROI) 1 mm wide along the length of the tube and dividing the mean absorption value for the voxels in the ROI by the background value. For the tomographic images we selected all voxels from the depth at which the contrast was greatest. Error bars represent the standard deviation of voxels in the ROI.
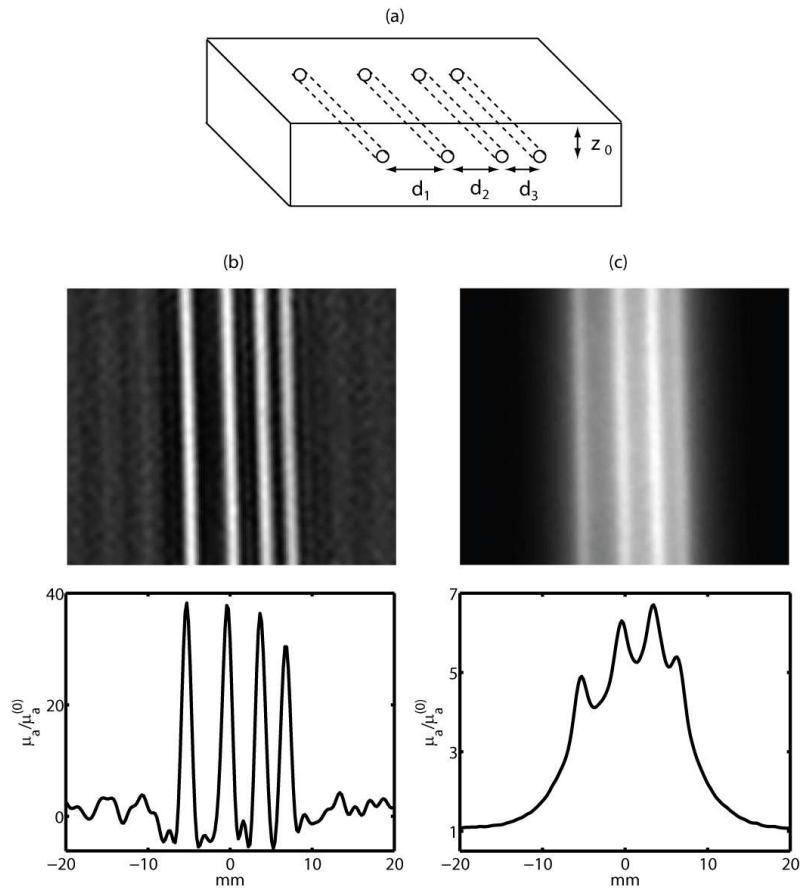
Fig. 4. (a) Schematic of tissue simulating phantom with four absorbing tubes located at a depth of $z_0 = 2$ mm, and with lateral separations of $d_1 = 5$ mm, $d_2 = 4$ mm, and $d_3 = 3$ mm. (b) Image and line profile of the reconstructed image using the tomographic method. (c) Image and line profile of the image produced by fitting to a homogeneous model.

Regardless of depth or imaging method, all curves are linear up to a contrast of 30:1, and then begin to saturate as expected due to the non-linearity of the inverse problem for diffuse light. We note that for this experiment, the linear range for tomographic reconstruction was larger than in previous work by a factor of about three [14]. However, non-linearity is expected to be more severe as the size of the inclusion becomes larger. Here the absorbing tube has a thickness of 1.5 ℓ^*, where as in the previous work the thickness of the absorber was 13 ℓ^*. Within the linear range both methods accurately give the relative change in contrast between the absorber and the background. However, the tomographic method comes closer to the actual values. Within the linear range, the percent error in measured absorption (i.e. 100 x (measured – expected)/expected) had a mean value of −2% and −28% at depths 2 mm and 3 mm respectively using the tomographic method.

The slight decrease in resolution at 3 mm suggests that the decrease in contrast measured at 3 mm is in part due to a partial volume effect. That is, the 3 mm tube appears broader and less intense due to the fact that the sensitivity of each detector is sharply peaked at the surface, and becomes both broader and smaller in magnitude with depth. While the reconstruction algorithm accounts for this effect, it does not remove it completely. Unlike the maximum absorption value, the total amount of reconstructed absorption does remain relatively constant with the depth of the tube. By integrating the reconstructed absorption of the entire tube, the total amount of reconstructed contrast is equal for the 2 mm and 3 mm depths to within 10%.

In contrast, when fitting pixel by pixel to a homogeneous model the absolute values of absorption are underestimated by up to a factor of about ten. This was expected, since the trajectories of the detected photons are primarily located in background medium, and not in the absorbing tube.
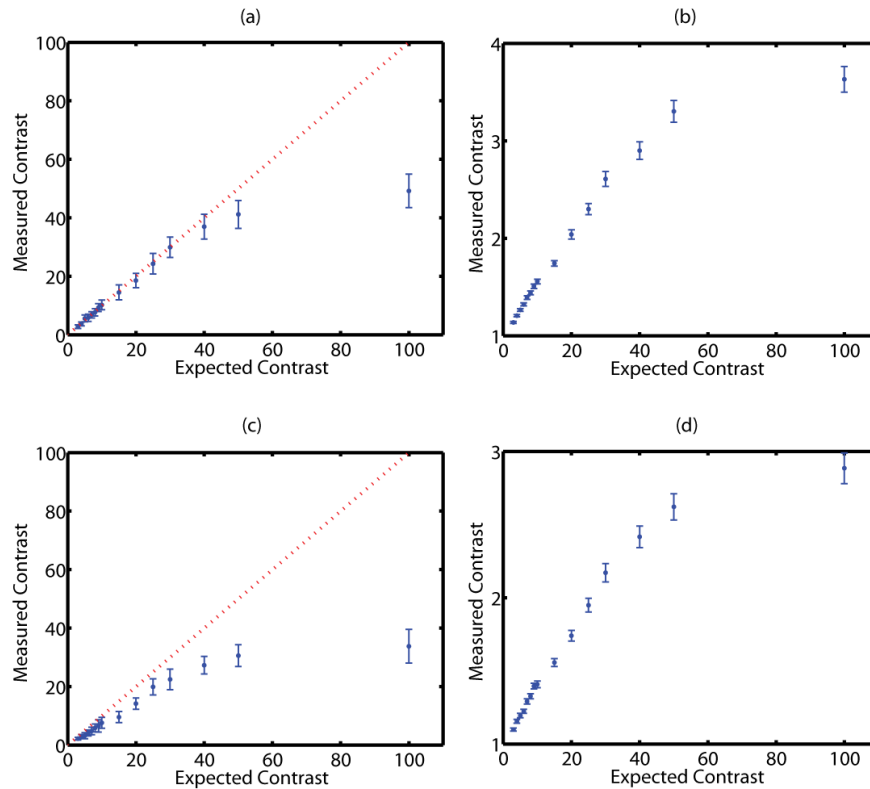

Fig. 5. Plot of measured (reconstructed) vs. expected (known) contrast for absorbing tubes whose contrast ranged from 3:1 to 100:1 at depths of (a,b) 2 mm and (c,d) 3 mm. The tomographic method was used in (a) and (c), whereas (b) and (d) were calculated by fitting to a homogeneous model. Error bars denote the standard deviation of voxels within a region of interest (see text). The dotted line represents the known value.

We were able to determine the relative depths of absorbers, but not their absolute depths. Figure 6 show the depth profiles of the tomographic images of the single tubes at both depths. For clarity, only depth profiles for the 5x, 10x, 20x, 30x, and 50x concentrations are shown. The grey area denotes the range of depths at which the maximum absorption was reconstructed. For both the 2 and 3 mm depths, the reconstructed images underestimate the depth of the tube. The maximum absorption occurred from 0.6 to 0.7 mm and 0.9-1 mm for actual depths of 2 mm and 3 mm respectively. We attempted to use spatially varying regularization [24] to overcome this effect. However, for these particular experiments we found that the depth at which the tubes appeared in the image was more determined by our choice of regularization parameter, than by the actual depth of the absorber.
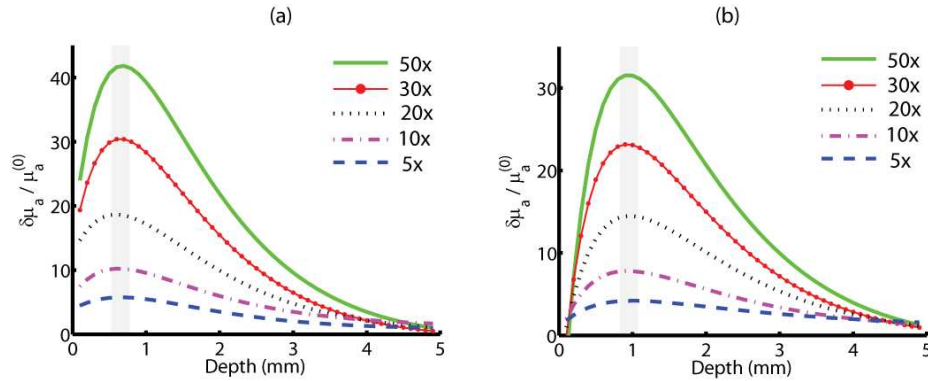
Fig. 6. Depth profiles of the three-dimensional images. For clarity only contrasts of 5x (dashed line), 10x (dash-dot line), 20x (dotted line), 30x (solid line with dots), and 50x (solid line) are shown. The grey area corresponds to the range in depth were the maximum values of absorption occur.

In these experiments the absorbers were located at 2-3 ℓ^* from the surface of the scattering medium, where the diffusion approximation to the radiative transport equation (RTE) is known to break down. It may be possible to more accurately determine the depths of buried absorbers by modeling photon transport using the RTE. Reconstruction algorithms such as the one used in this manuscript can be modified to incorporate radiative transport provided that the Fourier components of the Green's functions (see Eq. (7)) can be calculated for the RTE [25,26]. We are currently exploring the use of both analytic [27] and Monte Carlo methods to solve for these Fourier components. Use of the RTE may also result in more accurate quantification and improved resolution.

5. Conclusion

We used structured illumination to generate three-dimensional images of absorption contrast. The use of a new image reconstruction formula allowed us to obtain improved quantification which was linear up to contrasts of 30:1 for a small absorber similar to a superficial vein. It also led to a reduction in the full-width-half-maximum in the images of approximately a factor of three. We were able to determine the relative depths of the absorbers based on the reconstructed images, but always underestimated the absolute depth.

Acknowledgements